Research Article | Vol. 33, No. 5 / 10 Mar 2025 / Optics Express 10475
Optics EXPRESS

16-band single-photon imaging sensor based on Fabry-Perot resonance

CHUFAN ZHOU,[1,*] OLIVIER J. F. MARTIN,[2] AND EDOARDO CHARBON[1]

[1]Advanced Quantum Architecture Laboratory (AQUA), Ecole Polytechnique Federale de Lausanne (EPFL), 2002 Neuchatel, Switzerland
[2]Nanophotonics and Metrology Laboratory, Swiss Federal Institute of Technology Lausanne (EPFL), EPFL-STI-NAM, Station 11, CH- 1015 Lausanne, Switzerland
*chufan.zhou@epfl.ch

Abstract: We have demonstrated a 16 wavelength selective spectral bands imaging sensor-based Fabry-Perot (FP) structure for use in the near-infrared wavelength band (715 nm-915 nm). The designed structure consists of two symmetric SiC/SiO_2 distributed Bragg reflector (DBR) multilayer structures that sandwich a SiO_2 interval layer. We tuned the thickness of the SiO_2 interval layer to achieve wavelength selectivity and tunability. Fabrication and measurement results based on the FP structure show high resolution and good uniformity. Furthermore, for the first time, we combined the ultra-narrow band FP filter with single photon avalanche diode (SPAD). Finally, a category algorithm to reconstruct the narrow-band filter and improve the cross-talk caused by the overlap of the FP curve is proposed. The combination of FP hyper-spectral filter with SPAD opens the door to several novel applications.

1. Introduction

Multispectral imaging (MSI) and hyperspectral imaging have attracted great attention due to their potential applications in a variety of areas such as bio imaging [1–4], food science [5–7], and microscopy [8–10]. A traditional hyperspectral imaging system requires bulky dispersive optics or special tunable optical filters, which limit the system size and integration [11]. Integrated MSI system that can be used with wearable electronic devices in real-time have the potential to unleash many new MSI applications. Among those, snapshot imaging is a cutting-edge technology that enables the efficient acquisition of the spatial-spectral content, possibly using a miniaturized on-chip device [1,12–15]. Recent researches on the combination of MSI and deep learning technologies provide also novel methods to overcome the limitations of traditional MSI system such as bulky system size and low computational speed [16].

Fabry-Perot (FP) structures represent one of the workhorse approach to achieve wavelength selectivity and tunability [17–20]. A FP structure is a polarization-independent (for normal incidence) 1-D multilayer structure that contains at the top and bottom symmetrically distributed Bragg reflector mirror (DBR) sandwiching an interval cavity. A DBR is made up of periodic structures with high (n_H) and low refractive index (n_L) materials. The thickness of each DBR layer equals to a quarter of the optical wavelength. The thickness of the interval layer is equal to half of the optical length at the resonance wavelength. The existence of cavity breaks the perfect periodic system and permits localized mode to exist. Wavelength tunability can be achieved by changing the thickness of the cavity or modifying the refractive index in the cavity layer.

In this work, we report a single-photon avalanche diode (SPAD)-based [20,21] 16 band multi-spectral system. Instead of using a CMOS imaging sensor, we combined the SwissSPAD2 (SS2) and FP 16-band filter as a spectrometer system. SPADs are solid-state photodetectors that capture light at the single-photon level with high time resolution [21–23]. The SPAD technology has been widely studied and is used in several fields such as fluorescence lifetime

#551293 https://doi.org/10.1364/OE.551293
Journal © 2025 Received 20 Dec 2024; revised 27 Jan 2025; accepted 14 Feb 2025; published 28 Feb 2025

Optics EXPRESS

imaging (FLIM) [21–26], positron emission tomography (PET) [27], light detection and ranging (LIDAR) [28,29] and 3-D optical ranging [20,30]. The SS2 is designed with 512x512 pixels (it combines 512x256 top pixels with 512x256 bottom pixels, driven by two FPGA boards) with high sensitivity (50% photon detection probability (PDP) at a wavelength of 520 nm) and low dark count rate ($0.26 cps/\mu m^2$). The camera captures binary images with ideally no readout noise. SS2 has been utilized for FLIM [22,24]. Here, we report for the first time a prototype 16-band multi-spectral SS2, which takes its great potential from the combination of high spectral resolution with single-photon detection from the SPAD and could find applications in FLIM and clinical use. We also propose an algorithm for wavelength bands de-mixing.

2. Design and fabrication

2.1. Fabry-Perot resonance

We use the transfer matrix method to design and optimize the FP resonance structures; the full wave at half-maximum (FWHM) at the resonance wavelength is shown in Eq. (1), with m the resonance order, d the thickness of the interval layer, and R the DBR reflectance as detailed in Eq. (2). The refractive index of the substrate is n_{sub} while N represents the number of DBR pairs. According to Eq. (1), the FWHM is proportional to the thickness of the interval layer d. There are 3 methods to narrow down the FWHM: (a) increase the resonance order m, (b) increase the number N of DBR pairs, or (c) increase the contrast of the DBR material. Equation (3) represents the free spectral range (FSR) of the FP resonance, in other words, the operation wavelength range that we can tuned. Both the FSR and the FWHM are inversely proportional to the resonance order m; therefore, the FSR will decrease with the FWHM. The transmittance will also decrease as the number of pairs of DBR N increases due to the absorption of the chosen materials. By leveraging the transmittance, FWHM, and FSR, we designed a 4x4 array with 16 bands for hyperspectral imaging, with an operation wavelength range from 715 nm to 915 nm, and a uniform 12 nm spectral difference between neighbor peaks. The structures consists 2nd order resonance FP structures with SiC as high refractive index material (n_H) and SiO_2 as low refractive index material (n_L) in the DBR, and SiO_2 as interval layer material. According to the simulation results, the optimized thicknesses of SiC and SiO_2 in the DBR layer is 80 nm and 150 nm, respectively. The cavity thickness ranges from 450 nm to 675 nm with a 15 nm thickness difference between neighbor filter bands

$$FWHM = 2d\frac{1-R}{m^2\pi\sqrt{R}} \tag{1}$$

$$R = \left(\frac{1-\frac{n_H^{2N+2}}{n_L^{2N}n_{\text{sub}}}}{1+\frac{n_H^{2N+2}}{n_L^{2N}n_{\text{sub}}}}\right)^2 \tag{2}$$

$$FSR = \frac{2d(1-R)}{m\sqrt{R}} \tag{3}$$

Next, we fabricate and measure the spectral response of each filter band.

2.2. Fabrication process

We fabricated the 16 bands FP filter with four photolithography steps. As explained in the previous section, each band corresponds to one resonance wavelength and is achieved with a different cavity thickness. The fabrication process involves PECVD (Oxford Plasmalab System 100), photolithography (Heidelberg Instruments VPG200) and SiO_2 sputtering (Pfeiffer SPIDER 600). Figure 1 illustrates the fabrication process flow. First, we deposit the bottom DBR

Optics EXPRESS

pairs with PECVD at 300°C without breaking the vacuum (1000 m Torr), we spin coat the photoresist (Fig. 1(b)), and then follows the photolithography and SiO_2 deposition steps with sputter (Fig. 1(c)). The operation wavelength range was designed from 715 nm to 915 nm. We choose to use 2nd resonance FP structures and 3.5 pair SiC/SiO_2 DBR to achieve both a narrow spectral resolution and a high transmittance. We use SiC as high refractive index material and SiO_2 as low refractive index material. The cavity thicknesses range from 450 nm to 675 nm with 15 nm thickness difference between neighbor filter bands. To achieve a high uniformity of the resonance wavelength bands, we carefully control the deposition time of the SiO_2 cavity. The thickness of each deposition, ΔT, $\Delta T/2$, $\Delta T/4$, $\Delta T/8$ is 120 nm, 60 nm, 30 nm and 15 nm, respectively. Lastly, we deposit the top DBR with the same process as the bottom DBR. Figure 1(c, right) shows the four masks used for the photolithography steps. The top DBR is same as the bottom one.

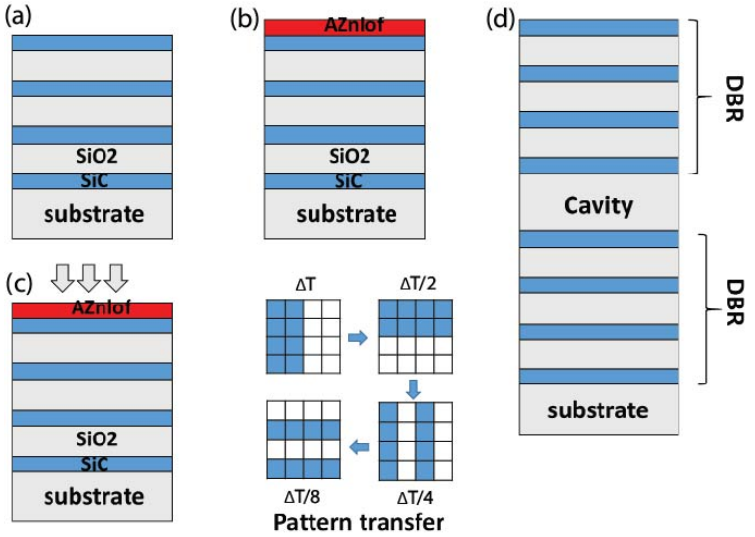

Fig. 1. Schematic of the fabrication process. (a) Deposition if the bottom SiC/SiO_2 DBR with PECVD on top of the substrate. (b) Spin coating of the photoresist for photolithograph. (c) Deposition of the interval SiO_2 layer with designed mask. The photolithography and deposition processes are repeated 4 times with 4 different masks. (d) Deposition of the top DBR with PECVD. The top DBR is the same as the bottom DBR

3. Result and discussion

3.1. Optical response of the fabricated filter

Figure 2 shows the simulation and measurement results for the 16 bands FP structure. Figure 2(a) shows the schematic of one single FP filter structure, all the data are simulated and measured under un-polarized normal incident light. Figure 2(b) top is the simulated transmittance for the 16 bands FP filter with different interval layers. The operation wavelength range from 715 nm to 915 nm with uniform 12 nm intervals between each peak. The wavelength tunability is achieved by increasing the thickness of the interval layer. Optical density (OD) here represents the wavelength selectivity shown in the following equation. I represents the intensity of light after it passes through the sample, I_0 is the intensity of the light before it enters the sample.

$$OD = \log_{10}\left(\frac{I_0}{I}\right) \tag{4}$$

Optics EXPRESS

Figure 2(b) bottom shows the simulated OD of each band, which falls in between 2-3 for each band. Figure 2(c) top is the transmittance measured by spectroscopy (FilMetrics F20-UV) at normal incidence, the spectral distance between neighbor peaks ranges around 11-13 nm. Figure 2(c) bottom shows the measured OD for each filter. The measured OD of each band falls in between 2-3. From these results, we conclude that experimental results on the effectively fabricated structures agree very well with the simulation results. This can be attributed to the fact that the thickness of each layer is well-controlled with our cleanroom fabrication process. Nevertheless, the measured transmittance at short wavelengths is lower than the simulation results due to the absorptance of SiC. The FWHM of the measured spectral response range between 5-10 nm. The measured results agree with the theory that the FWHM is increasing with the thickness of the interval layer. The detailed FWHM and center wavelength data are shown in the Supplement 1.

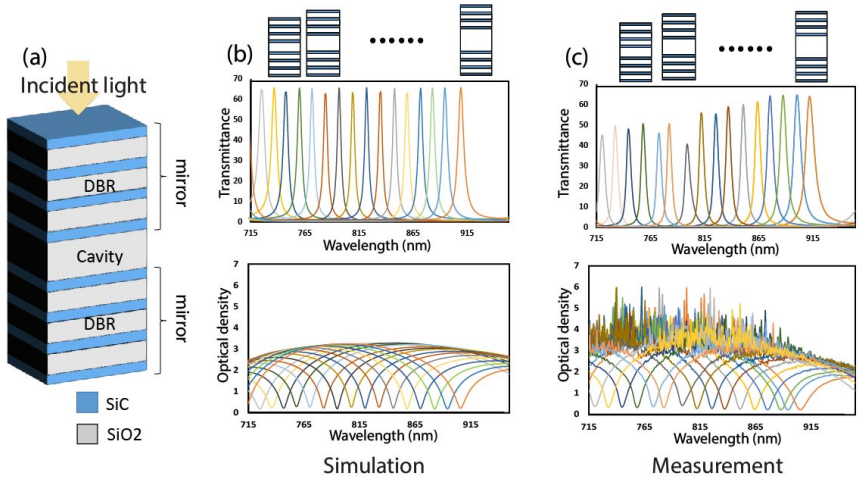

Fig. 2. (a) Schematic of the FP structure for one single pixel. The symmetric DBR consists of SiC as high refractive index material and SiO_2 as low refractive index material. (b) Top: simulated transmittance for 16 bands; bottom: simulated optical density; all simulations are performed with the transfer matrix method. (c) Top: measured transmittance of 16 bands with spectroscopy. The FWHM of each band ranges between 5-10 nm. Bottom:optical density for the 16 bands measured by spectroscopy. The optical density falls between 2-3.

3.2. Optical response in combination with SS2

We further combine the FP filter with the SS2 to achieve a prototype SPAD-based multi-spectral system. First we simulated and measured the photon response of the SS2 behind the FP filters, as described in the following and illustrated in Fig. 3. Figure 3(a) is the transmittance of the 16 bands FP filter measured with spectroscopy, while Fig. 3(b) is the measured PDP of the SS2 from literature [31], we take data at an excess bias of 12 V and assume the fill factor equals to 1. The measurement results end at approximately 850 nm. In our simulation, we assume that the measurment beyond 850 nm are equal to the value at 850 nm. Figure 3(c) shows the simulated photon response obtained by the dot product of the transmittance of the filter and the PDP of the SS2. In Fig. 3(a), the shorter wavelength band (715-815 nm) has lower transmittance than the longer wavelength band (815-915 nm) because SiC has less absorption for long wavelengths. After multiplication with the the PDP of the SS2, the photo response of the combined system will become higher at the lower wavelength, Fig. 3(c).

Optics EXPRESS

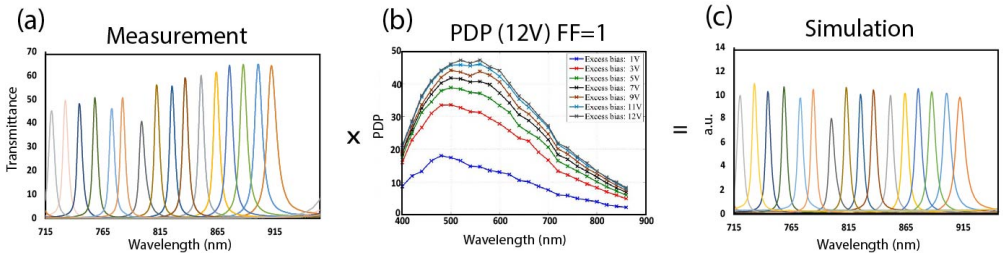

Fig. 3. (a) Measured transmittance of 16 bands with the spectroscopy. (b) Photon detection probability (PDP) of the SS2. Reprinted with permission from C. Veerappan and E. Charbon, IEEE Trans. Electron Devices 63(1), 65–71 (2016) [31]. (c) Simulated photon response resulting from the combination of the two.

Then we characterize the photon response performance of the combined system by measuring its response at different wavelength ranges between 715 nm and 915 nm. Figure 4(a) shows the schematic setup that combines the SS2 with the 16 bands filter. A supercontinuous laser (SuperK FIANIUM) is used to generate broadband illumination. A narrow band acousto-optic tunable Filter (SuperK VARIA A301-100-000) with a channel bandwidth of about 2-4 nm is connected to the continuous laser. We first fabricate a set of 4x4 16-band filters on a 4-inch wafer as described in Sec.2 with each band having a physical size of 3 mm x 3 mm (Fig. 4(a), right), 16 peak wavelengths are written on each square. This design facilitate the setup and measurement process. Two lenses are used to sequentially focus on the each filter (square). Then a diffuser is used to spread light evenly onto the SS2 pixels. We first focus the light onto the top-left square of the filter array (first row, first column). By varying the incident wavelength with acousto-optic tunable filter, we record the photon count detected by the SS2 corresponding to the first filter. Subsequently, we shift the focus to the second square (first row, second column) and repeat the photon count measurements. This process is iterated for all 16 filters in the array. A laptop is connected to the FPGA for data processing and storage. We activate 1 FPGA of the SS2 and use the top pixels (512 x 256 pixels) to collect 8 frames per filter per wavelength and sum up all the photon counting of each pixel, the acquisition time of each frame is 1/128 second. Figure 4(b) shows the measured photon count with different filters. The measured results with the SS2 shows the same transition as the simulation results, whereby the SS2 has higher photon response at lower wavelengths, Fig. 3(c).

Figure 4(c) left shows the measured angle dependency of one single filter (filter peak wavelength at 783 nm under collimated illumination at normal incidence). Without altering the overall experimental setup, we rotate the wafer around z-axis between 0° and 40°, in 10° steps. At each angle, we varied the incident wavelength and recorded the photon counts using the SS2. This allowed us to systematically characterize the angular dependence of the filter's performance while maintaining consistency in the experimental conditions. Figure 4(d) shows the simulated angle dependency using the transfer matrix method. The resonance wavelength shifts to shorter wavelengths as the incident angle increases. The measurement results show the same blue shift as the simulation results, as indicated by the star markers shown on the simulation heatmap in Fig. 4(d); the measured resonance wavelengths at different incidence angles lie on the same position of heatmap. SS2 is also sensitive to angle dependency when used as a spectrometer.

One notable limitation is the system's sensitivity to angular dependency. Future iterations of the design could incorporate angular compensation techniques or utilize advanced optical structures. For instance, employing a long-focal-length focusing lens in the setup could generate quasi-parallel light, thereby reducing angular deviations and improving the system's overall performance.

Optics EXPRESS

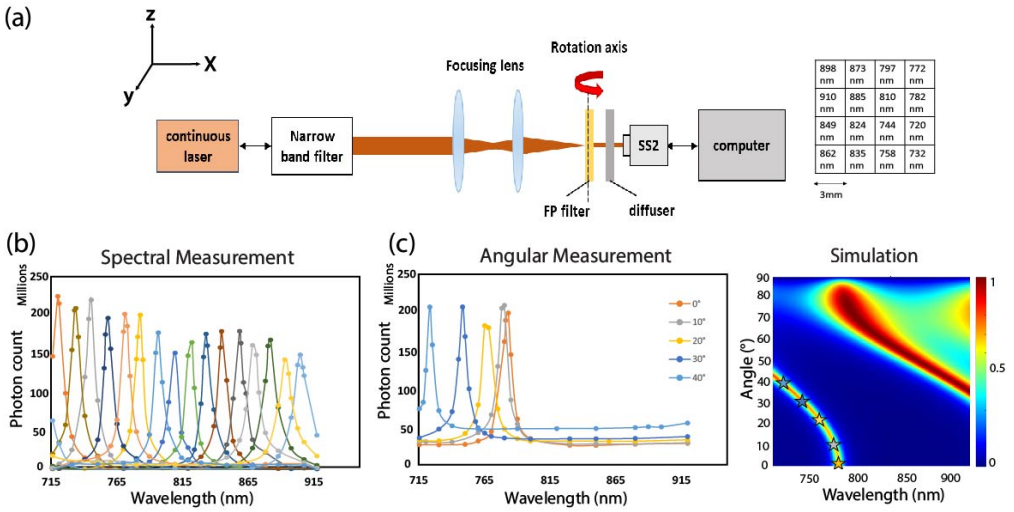

Fig. 4. (a) Measurement setup the combined system including the SS2 and FP filter. The filter is designed with 16 spectral bands fabricated on top of a 4 inch borofloat glass wafer, the size of each filter is 3 mm x 3 mm; the corresponding measured central wavelengths are shown on the right side. (b) Measured total photon count for different FP filters. (c) Spectral adjustment Measured Rotate the wafer around z axis and measure the angle dependency of FP structure. Left: Measured total photon count at the different angles 0°, 10°, 20°, 30° and 40°, respectively. Right: Simulated angle dependency. Measured results indicated as star markers agree with the simulation result that the resonance wavelength shifts to shorter wavelengths when the angle increases. Star markers on simulated angle dependency refers to the measured resonance wavelength at different angle.

Another key challenge lies in achieving higher transmittance in the visible spectrum, where the current material choices impose certain constraints. The use of more transparent materials, such as TiO_2/SiO_2 DBR, could enhance the optical throughput for shorter wavelengths. For applications requiring extended performance in longer wavelengths, materials such as Si/SiO_2 DBR present a promising alternative. These optimizations could improve the operational range and efficiency of the system, ensuring broader applicability across diverse imaging scenarios.

3.3. Spectral crosstalk evaluation

The current research on color crosstalk caused by spectral overlap has primarily focused on traditional RGB image sensors. Many studies have proposed solutions to address crosstalk. At the hardware level, the arrangement of filter patterns can be altered to minimize overlap between adjacent pixels as much as possible. This approach often requires customized design and then apply linear reconstruction algorithm focusing on crosstalk coefficient matrix [32,33]. Specifically, for each pixel, the corrected intensities of the RGB channels are estimated with the coefficient matrix. Here, we propose a similar method and discuss the pixel-scale integration approach in the Supplement 1. We plan to apply this reconstruction method to full integrated imaging in the future. On the other hand, the transmittance response of our FP structure exhibits a well-defined mathematical distribution. This unique characteristic allows us to leverage the known response function to calibrate crosstalk effectively. By utilizing the precise Lorentzian or Gaussian-like distribution of each filter, we can model the spectral crosstalk analytically and apply computational methods to correct it. This approach provides a distinct advantage over

Optics EXPRESS

traditional RGB systems, where the response profiles are less predictable and harder to model accurately.

The 16-band FP filter structure achieves a FWHM of 5–10 nm with a transmittance exceeding 40%, as confirmed both theoretically and experimentally. For FP structures, achieving narrower FWHMs typically involves increasing the number of DBR pairs or the thickness of the interval cavity layer. However, these adjustments often lead to reduced filter transmittance or a narrower FSR. To overcome the physical limitations of the FP structure, an alternative computational approach to spectral reconstruction is required. In this study, we employ the transfer matrix method to reconstruct the spectrum and subsequently apply the nearest-neighbor method to categorize photons [34,35]. As illustrated in Fig. 5(a), we first determine the resonance wavelength for each calibrated filter curve. Next, we define a new FWHM centered at the same resonance wavelength, setting FWHM = 3 nm in this instance, to ensure that the spectral lines do not overlap. Using these super-narrow response functions, we manually apply a transfer matrix to relate the measured spectrum to the reconstructed spectra, achieving high transmittance and precise spectral resolution.

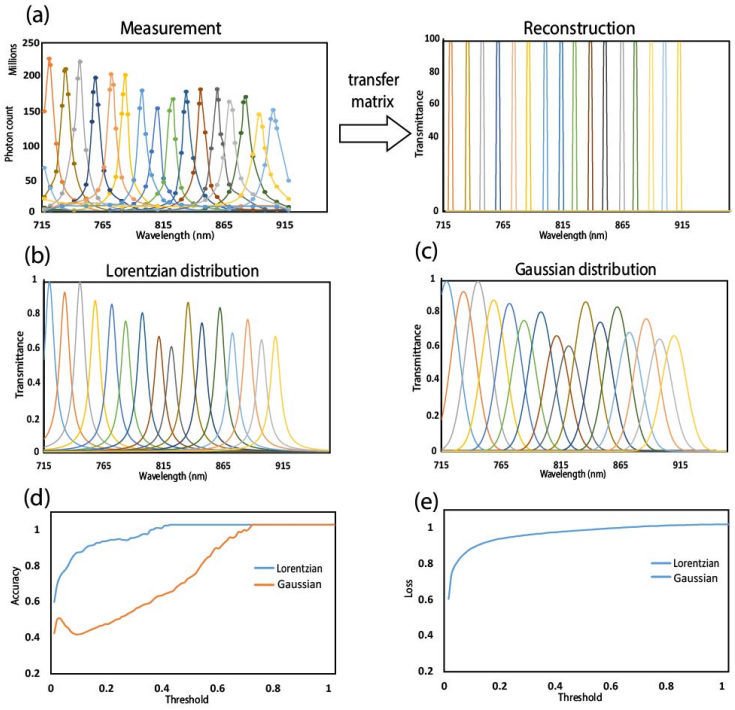

Fig. 5. (a) Applied transfer matrix to reconstruct the measured data (left) for narrow and high transmittance with FWHM 3 nm (right). (b) Reconstructed Lorentzian distribution model with FWHM at 10 nm. (c) Reconstructed Gaussian distribution with FWHM at 10 nm. (d) Category accuracy using Lorentzian function curve and Gaussian function curve. (e) Data losses during the category process.

However, cross-talk among neighboring FP curves becomes evident when the transmittance drops below 30%, resulting in overlap between adjacent bands. This overlap complicates the categorization of photons falling within the cross-talk region, as it becomes challenging to determine the corresponding band. To address this, a nearest-neighbor categorization algorithm has been developed to accurately classify photons in the overlap areas.

Optics EXPRESS

To implement this method, we first reconstruct Lorentzian and Gaussian function models, each with a FWHM of 10 nm around the resonance wavelength of each band, as illustrated in Fig. 5(b) and (c), respectively. By comparing 2 different models we aim to identify which is better suited our HSI system. The Lorentzian function is shown in Eq. (5), where x_0 is the center of the peak and Γ is the FWHM of the distribution. The Gaussian function, described in Eq. (6) is parameterized by real constant a and c, which controls the curve peak and curve width, respectively. The peak transmittance of each band is adjusted by the measured data to ensure accurate modeling.

$$L(x) = \frac{1}{\pi} \cdot \frac{\frac{\Gamma}{2}}{\left((x - x_0)^2 + \left(\frac{\Gamma}{2}\right)^2\right)} \tag{5}$$

$$G(x) = a \cdot \exp\left(-\frac{(x - x_0)^2}{2c^2}\right) \tag{6}$$

The nearest-neighbor categorization method is applied to measure data consisting of wavelength and normalized photon count to determine the best-fitting model for photon classification. For each data point, the nearest-neighor is identified on a Lorentzian or Gaussian distribution curve, and the geometrical distance between the measured point and the curve is calculated. This process is repeated across all 16 distribution curves, and the band number corresponding to the nearest-neighbor is assigned to the measured photon. The accuracy of the method is then evaluated by comparing the classification results from the Lorentzian and Gaussian models against known ground truth data. A manually defined intensity threshold is applied, considering only data points with intensities above the threshold in the calculation. Accuracy is defined as the proportion of correctly categorized data points above the threshold relative to the total number of such data points. This approach enables a direct comparison of the two models to determine which achieves higher accuracy in photon classification.

The categorization results, presented in Fig. 5(d) demonstrate that the nearest-neighbor method using the Lorentzian function model achieves significantly higher accuracy than the Gaussian model. When the threshold is set to 20%, the Lorentzian-based method reaches an accuracy of 90%, compared to only 32% for the Gaussian-based method at the same threshold. This indicates that the Lorentzian function model is highly effective in categorizing cross-talk photons that fall between neighboring bands. Furthermore, these findings corroborate previous research suggesting that the spectral line shape of FP filters closely resembles a Lorentzian distribution [36]. The data loss, defined as the proportion of measured data below the threshold, is shown in Fig. 5(e) and is found to be identical for both the Lorentzian and Gaussian models during the categorization process.

4. Conclusion

In summary, we demonstrate a FP based 16 bands ultra-narrow hyper-spectral imaging for SPAD operating at near-infrared spectral range, achieving a FWHM below 10 nm. Our study confirms that SS2 enables high spectral resolution and angular sensitivity when combined with an FP filter. Furthermore, we demonstrate category approach that integrates the transfer matrix method with the nearest-neighbor categorization method for spectral reconstruction. Through a comparative analysis of two models—the Lorentzian and Gaussian functions—we demonstrate that the Lorentzian function model is better suited to our 16-band multi-spectral system, which agree with the physical property of FP structure. The integration of SPAD and multi-spectral imaging (MSI) systems opens the door to a new generation of imaging devices. These systems can simultaneously capture 3D information (spatial and spectral) and, with SPAD's high time resolution, enable 4D data acquisition (2D spatial, spectral, and temporal) in a single shot.

Optics EXPRESS

Additionally, a minimized on-chip multi-spectral imaging system has broad potential applications, including ultra-compact multi-spectral FLIM and clinical applications.

Disclosures. The authors declare no conflicts of interest.

Data availability. Data underlying the results presented in this paper are not publicly available at this time but may be obtained from the authors upon reasonable request.

Supplemental document. See Supplement 1 for supporting content.

References

1. Z. Yang, T. Albrow-Owen, W. Cai, *et al.*, "Miniaturization of optical spectrometers," Science **371**(6528), eabe0722 (2021).
2. G. Lu and B. Fei, "Medical hyperspectral imaging: a review," J. Biomed. Opt. **19**(1), 010901 (2014).
3. T. Vo-Dihn, D. Stokes, M. Wabuyele, *et al.*, "A hyperspectral imaging system for in vivo optical diagnostics," IEEE Eng. Med. Biol. Mag. **23**(5), 40–49 (2004).
4. M. Manley, "Near-infrared spectroscopy and hyperspectral imaging: non-destructive analysis of biological materials," Chem. Soc. Rev. **43**(24), 8200–8214 (2014).
5. Y.-Z. Feng and D.-W. Sun, "Application of Hyperspectral Imaging in Food Safety Inspection and Control: A Review," Crit. Rev. Food Sci. Nutr. **52**(11), 1039–1058 (2012).
6. B. Park and R. Lu, eds., *Hyperspectral Imaging Technology in Food and Agriculture*, Food Engineering Series (Springer New York, 2015).
7. B. Wang, J. Sun, L. Xia, *et al.*, "The Applications of Hyperspectral Imaging Technology for Agricultural Products Quality Analysis: A Review," Food Rev. Int. **39**(3), 1–20 (2021).
8. S. J. Leavesley, N. Annamdevula, J. Boni, *et al.*, "Hyperspectral imaging microscopy for identification and quantitative analysis of fluorescently-labeled cells in highly autofluorescent tissue," J. Biophotonics **5**(1), 67–84 (2012).
9. R. A. Schultz, T. Nielsen, J. R. Zavaleta, *et al.*, "Hyperspectral imaging: A novel approach for microscopic analysis," Cytometry **43**(4), 239–247 (2001).
10. W. Jahr, B. Schmid, C. Schmied, *et al.*, "Hyperspectral light sheet microscopy," Nat. Commun. **6**(1), 7990 (2015).
11. D.-W. Sun, ed., *Hyperspectral imaging for food quality analysis and control* (Academic Press, an imprint of Elsevier, 2010), 1st ed. OCLC: ocn515496655.
12. A. Lambrechts, P. Gonzalez, B. Geelen, *et al.*, "A CMOS-compatible, integrated approach to hyper- and multispectral imaging," in *2014 IEEE International Electron Devices Meeting*, (IEEE, San Francisco, CA, USA, 2014), pp. 10.5.1–10.5.4.
13. K. Monakhova, K. Yanny, N. Aggarwal, *et al.*, "Spectral DiffuserCam: lensless snapshot hyperspectral imaging with a spectral filter array," Optica **7**(10), 1298 (2020).
14. B. Geelen, N. Tack, and A. Lambrechts, "A compact snapshot multispectral imager with a monolithically integrated per-pixel filter mosaic," (San Francisco, California, United States, 2014), p. 89740L.
15. B. Geelen, C. Blanch, P. Gonzalez, *et al.*, "A tiny VIS-NIR snapshot multispectral camera," (San Francisco, California, United States, 2015), p. 937414.
16. L. Huang, R. Luo, X. Liu, *et al.*, "Spectral imaging with deep learning," Light: Sci. Appl. **11**(1), 61 (2022).
17. K. Hirabayashi, Y. Ohiso, and T. Kurokawa, "Polarization-independent tunable wavelength-selective filter using a liquid crystal," IEEE Photonics Technol. Lett. **3**(12), 1091–1093 (1991).
18. G. Hernandez, *Fabry-Perot interferometers*, no. 3 in Cambridge studies in modern optics (Cambridge University, 2011), 1st ed.
19. J. M. Vaughan, *The Fabry-Perot interferometer: history, theory, practice, and applications*, The Adam Hilger series on optics and optoelectronics (A. Hilger, 1989).
20. F. Villa, R. Lussana, D. Bronzi, *et al.*, "CMOS Imager With 1024 SPADs and TDCs for Single-Photon Timing and 3-D Time-of-Flight," IEEE J. Sel. Top. Quantum Electron. **20**(6), 364–373 (2014).
21. C. Bruschini, H. Homulle, I. M. Antolovic, *et al.*, "Single-photon avalanche diode imagers in biophotonics: review and outlook," Light. Sci. Appl. **8**(1), 87 (2019).
22. A. C. Ulku, C. Bruschini, I. M. Antolovic, *et al.*, "Phasor-based widefield FLIM using a gated 512×512 single-photon SPAD imager," in *Multiphoton Microscopy in the Biomedical Sciences XIX*, A. Periasamy, P. T. So, and K. K. König, eds. (SPIE, San Francisco, United States, 2019), p. 21.
23. D. Bronzi, F. Villa, S. Tisa, *et al.*, "SPAD Figures of Merit for Photon-Counting, Photon-Timing, and Imaging Applications: A Review," IEEE Sens. J. **16**(1), 3–12 (2016).
24. A. C. Ulku, C. Bruschini, I. M. Antolovic, *et al.*, "A 512 × 512 SPAD Image Sensor With Integrated Gating for Widefield FLIM," IEEE J. Sel. Top. Quantum Electron. **25**(1), 1–12 (2019).
25. J. L. Lagarto, F. Villa, S. Tisa, *et al.*, "Real-time multispectral fluorescence lifetime imaging using Single Photon Avalanche Diode arrays," Sci. Rep. **10**(1), 8116 (2020).
26. A. Ghezzi, A. Farina, A. Bassi, *et al.*, "Multispectral compressive fluorescence lifetime imaging microscopy with a SPAD array detector," Opt. Lett. **46**(6), 1353 (2021).
27. M.-A. Tetrault, E. D. Lamy, A. Boisvert, *et al.*, "Real-Time Discrete SPAD Array Readout Architecture for Time of Flight PET," IEEE Trans. Nucl. Sci. **62**(3), 1077–1082 (2015).

Optics EXPRESS

28. C. Zhang, S. Lindner, I. M. Antolovic, *et al.*, "A 30-frames/s, 252 x 144 SPAD Flash LiDAR With 1728 Dual-Clock 48.8-ps TDCs, and Pixel-Wise Integrated Histogramming," IEEE J. Solid-State Circuits **54**(4), 1137–1151 (2019).
29. A. R. Ximenes, P. Padmanabhan, M.-J. Lee, *et al.*, "A 256×256 45/65nm 3D-stacked SPAD-based direct TOF image sensor for LiDAR applications with optical polar modulation for up to 18.6dB interference suppression," in *2018 IEEE International Solid - State Circuits Conference - (ISSCC)*, (IEEE, San Francisco, CA, 2018), pp. 96–98.
30. D. Bronzi, Y. Zou, F. Villa, *et al.*, "Automotive Three-Dimensional Vision Through a Single-Photon Counting SPAD Camera," IEEE Trans. Intell. Transport. Syst. **17**(3), 782–795 (2016).
31. C. Veerappan and E. Charbon, "A Low Dark Count p-i-n Diode Based SPAD in CMOS Technology," IEEE Trans. Electron Devices **63**(1), 65–71 (2016).
32. Y. Ye, H. Li, G. Li, *et al.*, "A crosstalk correction method to improve multi-wavelength LEDs imaging quality based on color camera and frame accumulation," Sig. Process.: Image Commun. **102**, 116624 (2022).
33. P. Wang and R. Menon, "Computational multispectral video imaging [Invited]," Journal of the Optical Society of America A **35**(1), 189 (2018).
34. N. Ismail, C. C. Kores, D. Geskus, *et al.*, "Fabry-Pérot resonator: spectral line shapes, generic and related Airy distributions, linewidths, finesses, and performance at low or frequency-dependent reflectivity," Opt. Express **24**(15), 16366 (2016).
35. P. Cunningham and S. J. Delany, "k-ACM Comput. Surv.," ACM Computing Surveys **54**(6), 1–25 (2022).
36. C. Kim, P. Ni, K. R. Lee, *et al.*, "Mass production-enabled computational spectrometers based on multilayer thin films," Sci. Rep. **12**(1), 4053 (2022).